

Force Generation Mechanisms by an Insect Wing in an Idealized Hovering Motion

H. R. Hamdani, A. Aizaz[†] and M. A. Naqvi

Aerospace Engineering Department, College of Aeronautical Engineering, National University of Sciences and Technology, Pakistan

[†]*Corresponding Author Email: ahmadaizaz@cae.nust.edu.pk*

(Received December 2, 2015; accepted October 7, 2016)

ABSTRACT

An Unsteady force generation mechanisms (delayed stall, wake capture and rotational lift) during idealized hovering of insect flight at Reynolds number (Re) of 136 have been identified in this research. Dependence of flow physics on Re forms the basis of present study to observe the dependence of unsteady force generation mechanisms on Re . A systematic study has been carried out by increasing Re from 136 to 4000 to investigate persistence of delayed stall, wake capture and rotational lift phenomenon. Using the solution of 3D Navier-Stokes equations, the aerodynamic force and the detailed flow structure around the wing are obtained which can provide useful insights into mechanism of unsteady force generation during idealized hovering at $Re=4000$. After grid and Mach number sensitivity analysis, the results are compared with previous studies at $Re=136$ for the code validation. The aerodynamic force and flow structure of a wing performing hovering motion at $Re=4000$ is calculated by solving Navier-Stokes equations. $Re=4000$ is selected on the premise that the length scale (mean aerodynamic chord) becomes closer to a Micro Air Vehicle (MAV); furthermore 30 times increase in Re (from 136 to 4000) is considered sufficient to assess changes in flow physics while remaining in laminar flow regime. Calculations are conducted for idealized hovering motion during which stroke 1 is initiated in still air, followed by flipping motion for reversing the direction and then stroke 2 (similar to stroke 1 but in opposite direction). Results obtained from this research are helpful for future work where they can be compared with those obtained from actual wing kinematics to assess the impact of kinematics on unsteady mechanisms.

Keywords: Hovering; Delayed stall; Wake capture; Insect flight; Low Reynolds number; CFD; Unsteady mechanism; Flapping wing; Wing kinematics.

NOMENCLATURE

a_∞	speed of sound	M_∞	free stream Mach number
c	mean chord length	Re	Reynolds number
C_D	drag coefficient	U_∞	free-stream reference velocity
\hat{C}_D	time averaged drag coefficient	α	angle of attack
C_L	lift coefficient	τ	non-dimensional time
\hat{C}_L	time averaged lift coefficient	τ_a	non-dimensional time for acceleration
l	radial position along the wing length from axis of rotation	ψ	azimuth rotation angle
DSV	dynamic stall vortex force MAV micro air vehicle	$\dot{\psi}$	angular velocity of azimuth rotation

1. INTRODUCTION

Flapping flight has always fascinated the

researchers and the curiosity has increased manifold due to interest in developing an electromechanical device capable of mimicking Flapping-flying insects. Flapping-flying insects

employ unsteady aerodynamic mechanisms to keep them afloat, and there have been many studies on this topic like Ellington (1984a), Ellington (1984b), Ellington (1984c), Ellington (1984d), Ellington et.al (1996), Van den Berg and Ellington (1997a), Van den Berg and Ellington (1997b), Dickinson et.al (1999), Liu (2002), Liu (2005), Sane (2003), Lehman (2004a), Lehman (2004b) and Wang (2005). During the last few years, CFD has also been widely applied to studies concerning insect flight. For instance, Liu and Kawachi (1998), Liu et.al (1998), Sun and Tang (2002a), Sun and Tang (2002b), Wang et.al (2004), Liu (2005), Wu and Sun (2004), Sun and Yu (2006), Yanpeng and Sun (2008) and Hamdani and Sun (2000). A major conclusion from these studies is that insects obtain sufficient lift force to support their weight through vortices generated by the flapping wings. Among the many mechanisms involved in flapping insect flight, "delayed stall" which is featured by prolonged attachment of a leading-edge vortex or Dynamic stall vortex (DSV) on a wing, has been widely recognized as an important unsteady aerodynamic mechanism contributing to the enhancement of lift force generation. Other unsteady mechanisms might also contribute to force production in insect flight. Dickinson *et al.* (1999) suggested that rotational circulation and wake capture increased aerodynamic force during the rotational phase of wing motion. These studies have made significant contributions to the understanding of different aspects of the aerodynamic mechanisms involved in insect flight. In a study of Hikaru Aono *et al.* (2008), Computational Fluid Dynamics (CFD) study of the unsteady 3D near- and far-field vortex wake dynamics in a hovering fruit fly and their relation to lift force generation using biology inspired dynamic flight simulator was conducted. Comparing the computed results for the hovering hawkmoth and fruit fly, marked dependence of the spanwise flow and the delayed stall on Re was elucidated.

Hovering is the most extreme and demanding aspect of flapping wing during which insect stays aloft while having no mean translational motion. In the present work, CFD code has been developed to understand the instantaneous force generation and vortex structures during idealized hovering of a fruitfly wing. Computations are performed for Idealized hovering motion, which consists of a 1st stroke where wing accelerates from rest to a constant velocity (taken at location of second moment of wing area) followed by deceleration to a complete stop. The second phase of the motion involves pitching of the wing through 100 degrees (stroke reversal), which is followed by a third phase in which 2nd stroke (similar to the first stroke i.e. acceleration, constant speed azimuth rotation, and deceleration) is carried out. Similar motion has been studied at Re =136 by Sun and Tang (2002a) using CFD, while Dickinson *et al* (1999) performed experiments using robofly wing. It is important to mention that idealized hovering motion (different than actual wing kinematics) is selected since sequential stroke and flipping motions are neatly

segregated and evidence of presence (or absence) of unsteady force generation mechanisms (delayed stall, wake capture and rotational lift) can be identified with relative ease. Results obtained from idealized hovering can then be compared with those obtained from actual wing kinematics to assess the impact of kinematics on unsteady mechanisms (comparison shall be presented in upcoming research paper). Dependence of flow physics on Reforms the basis of present study, in which Re is increased to 4000 and the results are compared with previous studies by Sun and Tang (2002a) and Dickinson *et al* (1999) at Re = 136. Main focus is to investigate persistence of delayed stall, wake capture and rotational lift phenomenon by increasing Re from 136 to 4000. Using the solution of Navier-Stokes equations, the aerodynamic force and the detailed flow structure around the wing are obtained which can provide useful insights into mechanism of unsteady force generation during idealized hovering at Re=4000. The Reynolds number is chosen since this Re range has been used in many studies for MAVs such as by A Naderi *et al* (2015). It is pertinent to mention that Re=4000 is selected on the premise that the length scale (mean aerodynamic chord) becomes closer to a Micro Air Vehicle (MAV); furthermore 30 times increase in Re (from 136 to 4000) is considered sufficient to assess changes in flow physics while remaining in laminar flow regime.

2. COMPUTATIONAL METHOD

The three-dimensional compressible Navier-Stokes equations are numerically solved in the present study. The finite-difference method has been used to solve the Navier-Stokes Equations in accordance with the Beam-Warming Scheme. The algorithm is second-order time accurate, non-iterative and spatially factored. In the Beam-Warming scheme, the solution is marched in time using the following difference formula:

$$\begin{aligned} \Delta \hat{U}^n = & \frac{\theta_1}{1+\theta_2} \Delta \tau \frac{\partial}{\partial \tau} (\Delta \hat{U}^n) + \frac{\Delta \tau}{1+\theta_2} \frac{\partial}{\partial \tau} (\hat{U}^n) + \frac{\theta_2}{1+\theta_2} \Delta \hat{U}^{n-1} \\ & + O[(\theta_1 - \frac{1}{2} - \theta_2)(\Delta \tau^2) + \Delta \tau^3] \end{aligned} \quad (1)$$

where: -

$$\hat{U}^n = \hat{U}(n \Delta \tau) \text{ and } \Delta \hat{U}^n = \hat{U}^{n+1} - \hat{U}^n$$

This general time-difference formula can represent many of the standard difference schemes, if appropriate values of θ_1 & θ_2 are chosen. In the present work, the three point backward implicit scheme is used $\theta_1=1$ & $\theta_2=1/2$, which is second-order accurate in time. The final differenced form of the algorithm can be solved, as three step block tri-diagonal system, as follows:-

$$\begin{aligned} & \left\{ 1 + \frac{\theta_1 \Delta \tau}{1+\theta_2} \left[\frac{\partial}{\partial \xi} (A)^n - Re^{-1} \frac{\partial}{\partial \xi} \left(R_U^n - \frac{\partial}{\partial \xi} R_{U_\xi}^n \right) - Re^{-1} \frac{\partial^2}{\partial \xi^2} (R_{U_\xi}^n) \right] \right. \\ & \left. - \varepsilon \Delta \tau^{-1} \frac{\partial^2 J}{\partial \xi^2} \right\} \Delta U^* = RHS \\ & \left\{ 1 + \frac{\theta_1 \Delta \tau}{1+\theta_2} \left[\frac{\partial}{\partial \eta} (B)^n - Re^{-1} \frac{\partial}{\partial \eta} \left(S_U^n - \frac{\partial}{\partial \eta} S_{U_\eta}^n \right) - Re^{-1} \frac{\partial^2}{\partial \eta^2} (S_{U_\eta}^n) \right] \right. \end{aligned}$$

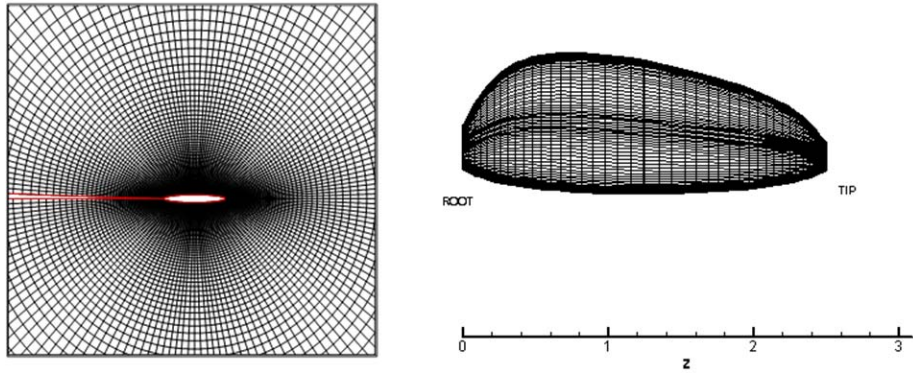


Fig. 1. A portion of the grid around a section and on the wing surface.

$$\begin{aligned}
 & -\varepsilon_e \Delta \tau^{-1} \frac{\partial^2 J}{\partial \eta^2} \} \Delta \bar{U} = \Delta U^* \\
 & \left\{ 1 + \frac{\theta_1 \Delta \tau}{1 + \theta_2} \left[\frac{\partial}{\partial \zeta} (C)^n - Re^{-1} \frac{\partial}{\partial \zeta} \left(H_U^n - \frac{\partial}{\partial \zeta} H_{U_\zeta}^n \right) - Re^{-1} \frac{\partial^2}{\partial \zeta^2} (H_{U_\zeta}^n) \right] \right. \\
 & \left. - \varepsilon_i \Delta \tau^{-1} \frac{\partial^2 J}{\partial \zeta^2} \right\} \Delta \hat{U}^n = \Delta \bar{U} \\
 (2)
 \end{aligned}$$

where

$$\begin{aligned}
 RHS = & \frac{\Delta \tau}{1 + \theta_2} \left\{ \frac{\partial}{\partial \zeta} \left[-\hat{E}^n + Re^{-1} (\hat{R}_1^n + \hat{R}_2^n + \hat{R}_3^n) \right] \right. \\
 & + \frac{\partial}{\partial \eta} \left[-\hat{F}^n + Re^{-1} (\hat{S}_1^n + \hat{S}_2^n + \hat{S}_3^n) \right] \\
 & + \frac{\partial}{\partial \zeta} \left[-\hat{G}^n + Re^{-1} (\hat{H}_1^n + \hat{H}_2^n + \hat{H}_3^n) \right] \\
 & + \frac{\theta_1 \Delta \tau}{1 + \theta_2} Re^{-1} \left[\frac{\partial}{\partial \zeta} (\Delta \hat{R}_2^{n-1} + \Delta \hat{R}_3^{n-1}) \right. \\
 & \left. + \frac{\partial}{\partial \eta} (\Delta \hat{S}_1^{n-1} + \Delta \hat{S}_3^{n-1}) \right. \\
 & \left. + \frac{\partial}{\partial \zeta} (\Delta \hat{H}_1^{n-1} + \Delta \hat{H}_2^{n-1}) \right] + \frac{\theta_2}{1 + \theta_2} \Delta \hat{U}^{n-1} \\
 & \left. + \left[-\varepsilon_e \Delta \tau^{-1} \left(\frac{\partial^4}{\partial \zeta^4} + \frac{\partial^4}{\partial \eta^4} + \frac{\partial^4}{\partial \zeta^4} \right) (J \hat{U}^n) \right] \right\}
 \end{aligned}$$

where, ε_e and ε_i are the coefficients of the explicit and implicit smoothing terms, respectively.

The Mach number is given a low value such that the solution is a close approximation to that of incompressible flow (further details presented in next section). The general transformations are used to transform the governing equations from the physical domain (x, y, z) to the computational domain (ξ, η, ζ): For flow past a body in arbitrary motion, the governing equations can be cast in an inertial frame of reference using a general time-dependent coordinate transformation to account for the motion of the body. Employing this approach, the Navier-Stokes equations are expressed in strong conservation form. They are well documented in the literature in Hikaru Aono *et.al* (2008) and will not be repeated here.

Conventional boundary conditions are applied everywhere. At the inflow boundary, the velocity

components and temperature are specified at free stream conditions while the pressure is extrapolated from the interior. At the outflow boundary, the pressure is set equal to the free-stream static pressure and the velocity and temperature are extrapolated from the interior. Along the grid cut-line, periodic boundary conditions are enforced. On the wing surface, adiabatic, impermeable wall and no-slip boundary conditions are applied, and the pressure on the boundary is obtained through the normal component of the momentum equation.

3. GRID GENERATION

Body-fitted O-H-type grid is constructed by spanwise stacking of 2-D O-type grids. The two-dimensional grid is generated by using a special Poisson solver based on the method of Thomas given by Beam and Warming (1978). A portion of the grid used for wing in spanwise and chordwise direction is shown in Fig. 1.

The three dimensional grid is constructed by spanwise stacking of two-dimensional O-type grids. For the stacking procedure, the mid span chord is used to normalize the wing under a 7th order polynomial for leading edge and a 6th order polynomial for the trailing edge. The resulting wing has a wing span (B) of 2.5 with aspect ratio (AR) 3.74 (Fig. 2).

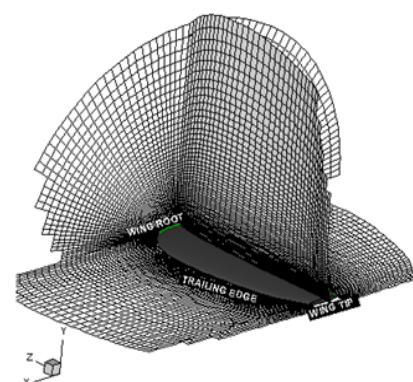


Fig. 2. Position of the O-H type Grid of the modified fruitfly wing (aspect ratio AR=3.74).

4. WING KINEMATICS, GRID AND MACH NUMBER SENSITIVITY

4.1 Model Wing Kinematics

In idealized hovering flight (Fig. 3), Stroke 1 starts by accelerating for τ_a in still air to some constant speed (U). Constant speed translation continues for few chord lengths of travel and then the wing decelerates to zero velocity in deceleration time (τ_d) to complete first translation (*stroke 1*). This is followed by flip motion (pitching) about axis of rotation ($0.25c$) by 100 degrees i.e. from 40° to 140° (stroke reversal). Stroke 2 then starts and the kinematics is similar to Stroke 1 (though the flow field is considerably changed due to wake of Stroke 1 and flipping motion). The translational speed, u_t , is equal to U during constant speed phase. During the acceleration and deceleration phases, u_t is given by:

$$u_t^+ = -0.5 \left[1 - \cos \left\{ \frac{\pi(\tau - \tau_1)}{\tau_a} \right\} \right]; \quad \tau_1 \leq \tau \leq \tau_a \quad (3)$$

$$u_t^+ = 0.5 \left[1 + \cos \left\{ \frac{\pi(\tau - \tau_2)}{\tau_d} \right\} \right]; \quad \tau_2 \leq \tau \leq \tau_d \quad (4)$$

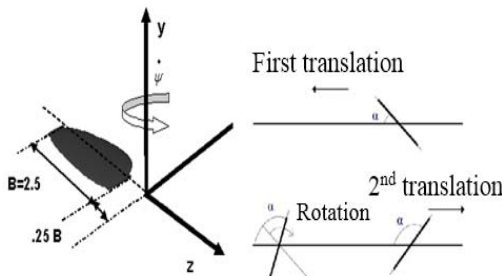


Fig. 3. Motion set up for the Fruit fly wing.

where, $u_t^+ = \frac{u_t}{U}$, $\tau = \tau U/c$ (equivalent to number of chord lengths travelled), c is the chord length of the wing and U is a reference velocity. The Reynolds number is defined as $Re = cU/v$ ('v' is the kinematic viscosity) and $Re = 4000$. The Mach number (based on U) is set as 0.1 (to be discussed further in next paragraph). The force coefficients, C_L and C_D , are defined as $C_L = L/(0.5\rho U^2 SC_{La})$ and $C_D = D/(0.5\rho U^2 SC_{La})$ respectively. Here, τ_1 and τ_2 are the non-dimensional times at which the acceleration and deceleration start in each stroke respectively. Denoting the azimuth rotation speed as ψ (which provides for $U = r_2 \dot{\psi}$), and where $r_2 = \left[\int_A r^2 \frac{dA}{A} \right]^{\frac{1}{2}}$ (second moment of wing area) was calculated as $0.58l$, where l is wing span (B) plus the distance between the wing root to the rotational axis ($0.25 B$). During flipping motion (stroke reversal), α changes with time, and the angular velocity, $(\dot{\alpha})$, is given by :

$$\dot{\alpha}^+ = 0.5\alpha_o^+ \left[1 - \cos \left\{ 2\pi(\tau - \tau_r)/\Delta\tau_r \right\} \right]; \quad \tau_r \leq \tau \leq \tau_r + \Delta\tau_r \quad (5)$$

where, $\dot{\alpha}^+ = \dot{\alpha}c/U$, α_o^+ is a constant representing maximum value of $\dot{\alpha}$, τ_r is the non-dimensional time at which the rotation starts and $\Delta\tau_r$ is the time interval over which the rotation lasts. During $\Delta\tau_r$, wing rotates from $\alpha = 40^\circ$ to $\alpha = 140^\circ$; therefore when either α_o^+ or $\Delta\tau_r$ are specified the other can be determined by the relation:-

$$\alpha_o^+ = (\alpha_{final} - \alpha_{start}) / 0.5\Delta\tau_r \quad (6)$$

In essence, there are five variables while considering the motion: Acceleration time (τ_a), Deceleration time (τ_d), Stroke amplitude in degrees (ψ), flip velocity ($\dot{\alpha} = \dot{\alpha}c/U$) and scheduling of Flipping motion. In the present study, following assumptions are made to reduce the number of variables:

- 1) Acceleration and deceleration time are kept equal and three cases are considered ($\tau_a = \tau_d = 0.5, 1.0$ and 1.5 corresponding to fast, medium and slow rates respectively).
- 2) Stroke amplitude (ψ) or azimuth angle is fixed as 155° .
- 3) Flip velocity ($\dot{\alpha} = \dot{\alpha}c/U$) is given three values ($\dot{\alpha} = 2.75, 2.0$ and 1.25 corresponding to fast, medium and slow rates respectively).
- 4) Flip scheduling is not catered for and flip motion commenced at the end of Stroke 1 and ended before the start of Stroke 2.

Calculations are then performed for various combinations of acceleration/deceleration time and flip rate, resulting into study of 9 cases. It is important to mention that neatly separated motions i.e. idealized hovering can provide useful insights and make foundation to understand the natural hovering during which there is an overlap between a stroke and pitch rotation.

4.2 Grid Sensitivity Study

For Grid independence study, the wing translation starts by accelerating for τ_a in still air (Eq. 1) to some constant speed U (denoted as Motion 1). Two grids are considered: Grid 1 is of the size $125 \times 72 \times 76$, in normal direction, around the wing section and in the spanwise direction respectively and Grid 2 of $156 \times 90 \times 76$. The far field boundary is set at 10 chord lengths away from the wing surface in the normal direction and 5 chord lengths away from the tip in the spanwise direction. The calculated lift and drag coefficients are shown in Fig. 4. It is seen that during the acceleration phase, there is almost no difference between the results of these two grids; during constant speed phase, there is very small difference between the results, which indicate that results of grid 1 and grid 2 are similar. From the above result, grid 2 is selected for the present study for ensuring more accuracy as well as better resolution of flow pictures.

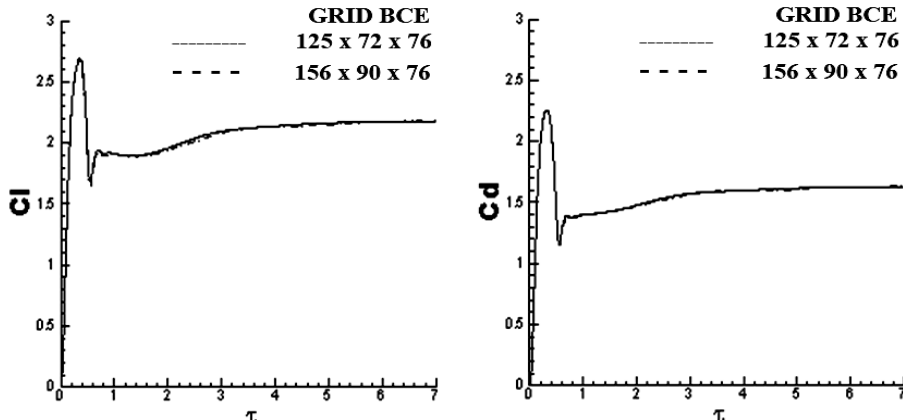


Fig. 4. Lift and Drag force coefficients plots versus τ for Grid 1 and 2.

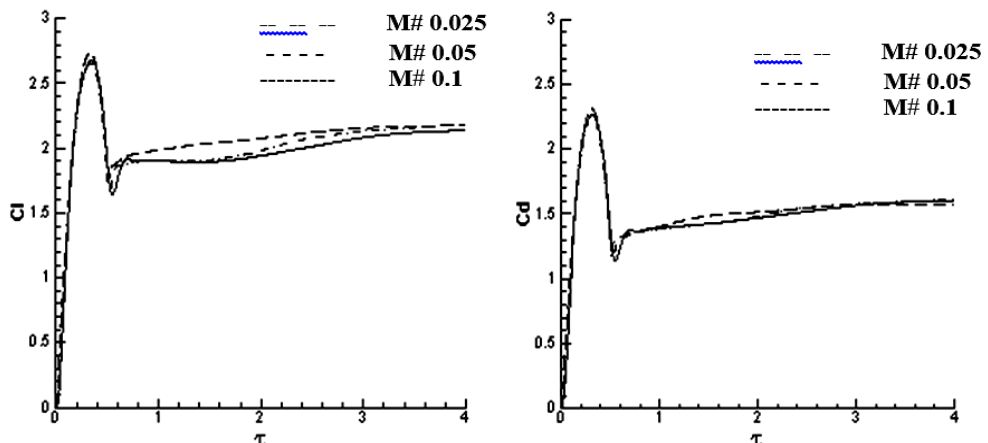


Fig. 5. Force coefficients vs τ for a wing performing Motion 1 at different Mach Numbers.

4.3 MACH NUMBER SENSITIVITY STUDY

In order to obtain solutions close to that of incompressible flow, the value of Mach number needed to be small enough so that compressibility effects do not affect the solution. For this purpose, calculations are performed for wing performing Motion 1. Calculations are performed at three Mach numbers, $M_\infty=0.1$, 0.05 and 0.025 at $Re = 4000$. Fig. 5 shows the lift (C_L) and drag (C_D) force coefficients at different Mach numbers and it is seen that the results for the three Mach numbers are similar during acceleration phase. In the constant speed phase, lower Mach number slightly gives higher lift coefficient as compared to $M_\infty=0.1$. Therefore, Mach 0.1 (33 ms^{-1}) is selected for subsequent computations since it would give a good approximation to that of incompressible flow at Mach number as low as 0.01 (3.3 ms^{-1}).

4.4 Code Validation

The code has been validated by comparing the results with experimental data at low Reynolds number, as given in Hamdani, H. and Sun, M.

(2000). Code validation is also performed by comparing the computational results with experimental results at $Re = 120$ and 1400 by Thomas (1982). Table 1 show the mean lift and drag coefficients at different angles of attack for experimental and computational results.

Table 1 Mean Force Coefficients: Experimental and Numerical Results for a wing in azimuth rotation after rapid acceleration

aoa α (deg)	experimental †		numerical ($\tau_a=0.5$)		% difference in \bar{C}_L
	\bar{C}_L	\bar{C}_D	\bar{C}_L	\bar{C}_D	
40	1.886	1.55	1.96	1.49	-3.9
30	1.7128	.938	1.72	.904	-0.11
20	1.205	.527	1.24	.429	-2.9
10	.6236	.274	.628	.154	-0.7

Figure 6 shows comparative force coefficient plots for the experimental and numerical results where, essentially the results are similar especially when α is small. Variation in results could be due to the

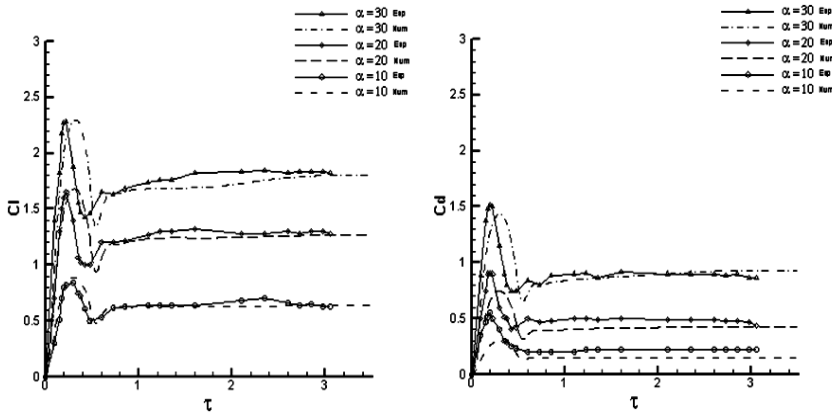


Fig. 6. Experimental (Dickinson et al.) and Numerical results of the Wing performing Motion 1.

different acceleration time used in experiment, which is not known from their reported work.

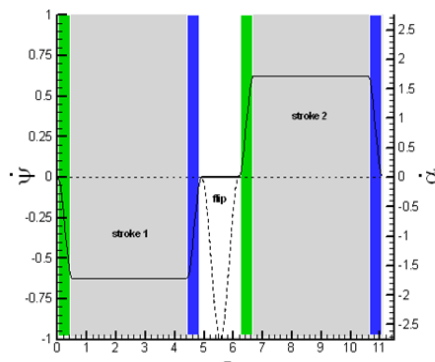


Fig. 7. Azimuth angular velocity and pitching angular velocity versus non dimensional time (τ).

5. RESULTS

5.1 Dealized Hovering Motion

Figure 7 shows the variation of azimuth rotation velocity ($\dot{\psi}$) and pitch angular velocity versus τ during one complete cycle. The green bar represents the acceleration time (τ_a), the blue bar represents the deceleration phase (τ_d) and grey portion represents the constant velocity phase during each stroke. The plot is for the representative case of $\tau_a = \tau_d = 0.5, \alpha_o^+ = 2.75$. The total non-dimensional time taken for one cycle (two strokes) is approximately 11.089. Table 2 gives the various combinations of α_o^+ and τ_a and τ_d (total nine cases) considered in this study. Each case is denoted by a combination of two alphabets (FF, FM, FS, MF, MM, MS, SF, SM and SS) where the first alphabet denotes the acceleration or deceleration rate during azimuth rotation, while second alphabet denotes the angular velocity rate during stroke reversal. For example, FS means fastest acceleration/deceleration and slowest pitching rate ($\tau_a = \tau_d = 0.5$ and $\alpha_o^+ = 1.25$) and MM means medium acceleration / deceleration and medium pitching rate

($\tau_a = \tau_d = 1.0$ and $\alpha_o^+ = 2.0$) etc. In the following sections, results of instantaneous force production are discussed in terms of time averaged force coefficients (\bar{C}_L and \bar{C}_D) and vorticity plots. It is important to mention that the time rate of change of total first moment of vorticity at an instant provides quantitative insight; however it has not been computed in the present study and only qualitative assessment is made using vorticity plots.

Table 2 Matrix of nine cases comprising of various combinations of α_o^+ and τ_a and τ_d

	Stroke 1 At $\alpha=40^\circ$	Slow (S)	Medium (M)	Fast (F)	Stroke 2 At $\alpha=140^\circ$
	$\tau_a=\tau_d$	α_o^+	α_o^+	α_o^+	$\tau_a=\tau_d$
Fast (F)	0.5	1.25	2.0	2.75	0.5
Medium (M)	1.0	1.25	2.0	2.75	1.0
Slow (S)	1.5	1.25	2.0	2.75	1.5

5.2 Force Production for Cases FF, FM and FS

Case FS kinematics is explained in detail for subsequent understanding of other cases. For the Stroke 1, the wing accelerates in still air ($\tau_1 = 0.0$) for ($\tau_a = 0.5$) and after translating in a constant speed phase for $\tau = 3.91$ ($\tau_2 = 4.41$), it decelerates to zero velocity (at $(\tau = 4.91)$ after completing an azimuth rotation of $\psi = 155^\circ$. At the end of stroke 1, the wing flip motion starts to rotate the wing at $\alpha_o^+ = 1.25$ or $\Delta\tau_r = 2.793$ for $\alpha = 100^\circ$ (stroke reversal).

The wing then starts the Stroke 2 with the same non dimensional time parameters as in stroke 1, however now $\tau_1 = 7.7025$ and $\tau_2 = 12.1125$ and at the end of stroke 2, $\psi = 0.0^\circ$. Fig. 8 shows the instantaneous force production during the complete cycle for Case FF. It can be seen that during the acceleration phase of Stroke 1, force coefficients closely follow the acceleration rate ($\dot{\psi}^+$) and

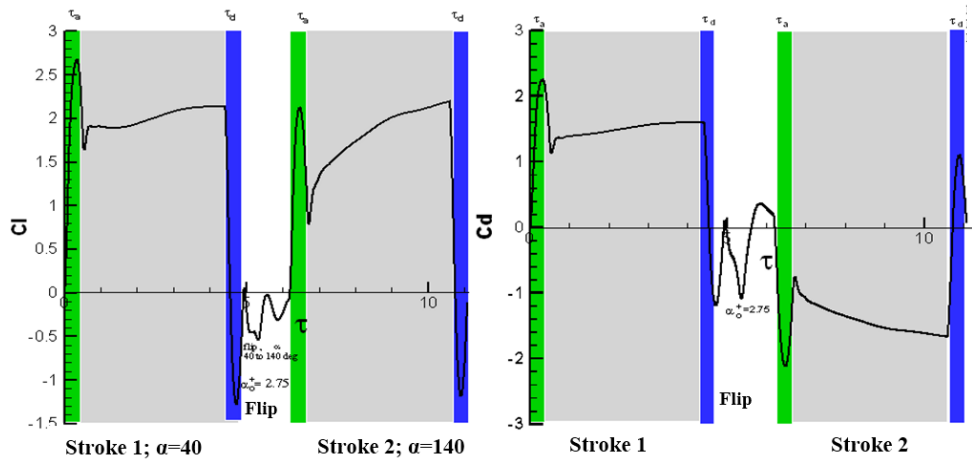


Fig. 8. Case FF; Lift and drag coefficient versus τ during the cycle
($\tau_a = \tau_d = 0.5$ and $\alpha_o^+ = 2.75$ or $\Delta \tau = 1.269$).

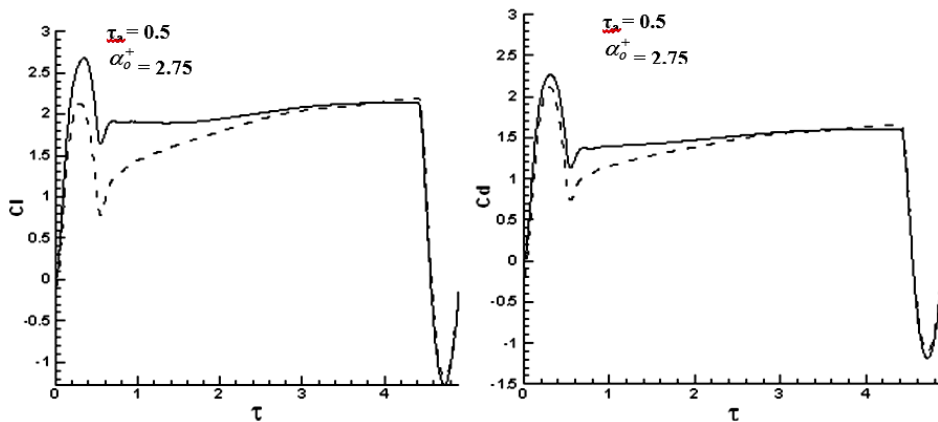


Fig. 9. Comparison between two strokes. Force coefficient versus non dimensional time τ for Case FF.
Solid and dashed lines represent stroke 1 and stroke 2, respectively.

achieve large force peaks. C_L peak of nearly 2.67 is achieved during acceleration and just after the acceleration ends, C_L drops to 1.64. From here on, the C_L rises gradually to new peak of C_L and exhibits a large constant value of C_L (greater than 2) at $\tau = 4.0$, ($\psi \square 130^\circ$). This large value of C_L is maintained throughout the constant speed phase and there is no sign of stall. Similar variation for C_D is seen from the C_D vs τ plot in Fig. 8.

The wing then decelerates to zero velocity (end of Stroke 1), C_L drops immediately and exhibits similar but opposite behaviour to acceleration phase. At the end of Stroke 1, C_L value is approximately zero. Flipping motion commences during which wing rotates at quarter chord point from $\alpha = 40^\circ$ to 140° . During flipping, C_L drops initially to a value of -0.5 and then becomes zero at $\alpha = 90^\circ$ but then another peak appears. At the end of flipping motion, C_L is again approximately zero. It is important to note that the flipping motion occurs in the midst of wake generated by Stroke 1.

It is interesting to investigate the effects of previous Stroke (i.e. Stroke 1) and flip on Stroke 2, which may provide insight into the other force generation

mechanisms namely ‘Wake Capture’ and ‘Rotational Lift’. During acceleration phase of Stroke 2, force coefficients rise rapidly to a large value till mid of acceleration. Subsequently C_L drops to a value of around 1.0. In the constant speed phase, C_L starts to increase continually till the end of constant speed phase but without forming any lift plateau, as opposed to the one formed during Stroke 1.

Table 3 shows the time averaged force coefficients for the 3 cases (FF, FM and FS). For case FF, \bar{C}_L and \bar{C}_D for stroke 1 are 1.77 and 1.32 respectively, but these values drop during stroke 2 with \bar{C}_L and \bar{C}_D as 1.59 and 1.24 respectively.

The difference between the two strokes is quite visible in Fig. 9. Here, the Stroke 2 can be seen producing lesser force during the acceleration phase and lags in force generation during the constant speed translation phase for nearly 3 chord lengths of travel.

C_L and C_D versus τ for case FM and FS are shown

Table 3 Mean and Maximum force coefficient production during Stroke 1 only, Stroke 1 combined with flip and Stroke 2 only for FF, FM and FS

CASE	FS				FM				FF			
$\tau_a = \tau_d = 0.5$	$\alpha_o^+ = 1.25$				$\alpha_o^+ = 2.0$				$\alpha_o^+ = 2.75$			
	\bar{C}_L	\bar{C}_D	$C_{L\max}$	$C_{D\max}$	\bar{C}_L	\bar{C}_D	$C_{L\max}$	$C_{D\max}$	\bar{C}_L	\bar{C}_D	$C_{L\max}$	$C_{D\max}$
Stroke 1	1.77	1.32	2.68	2.26	1.77	1.32	2.68	2.26	1.77	1.32	2.68	2.26
Stroke 2	1.62	1.25	2.28	2.11	1.60	1.24	2.20	2.12	1.59	1.24	2.20	2.11

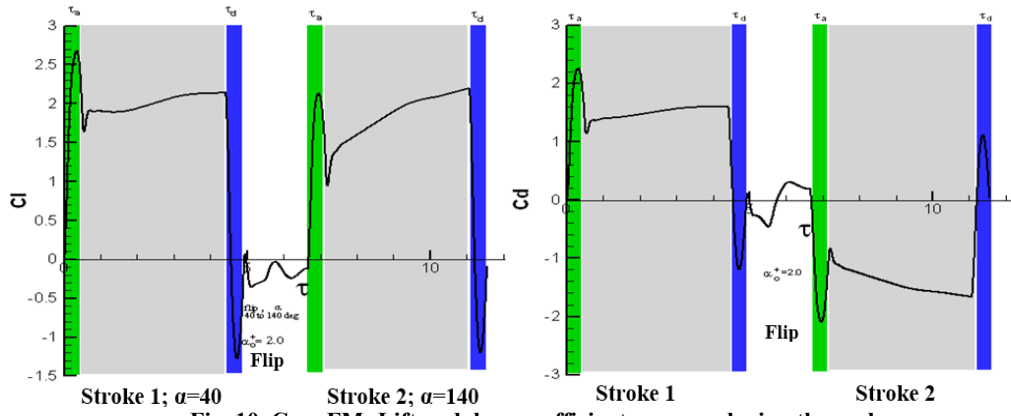


Fig. 10. Case FM: Lift and drag coefficient versus τ during the cycle

($\tau_a = \tau_d = 0.5$ and $\alpha_o^+ = 2.0$ or $\Delta\tau = 1.745$).

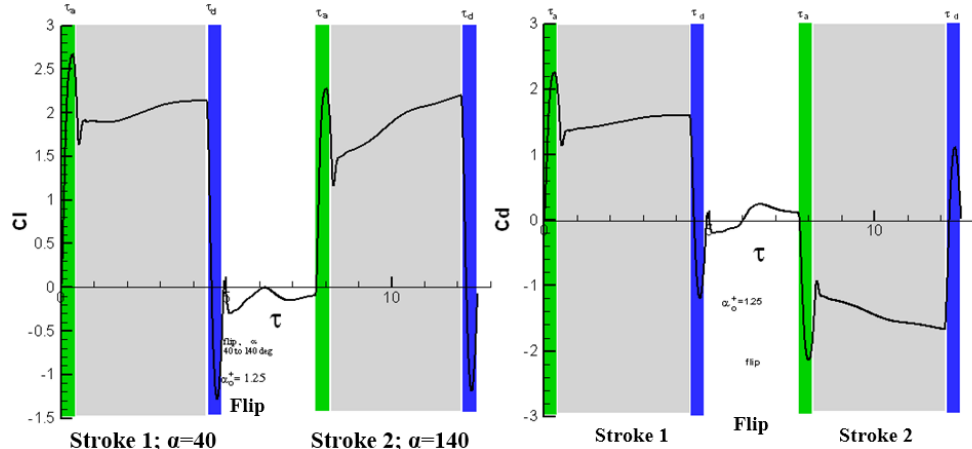


Fig. 11. Case FM: Lift and drag coefficient versus τ during the cycle

($\tau_a = \tau_d = 0.5$ and $\alpha_o^+ = 1.25$ or $\Delta\tau = 2.793$).

in Fig. 10 and 11 respectively. Despite variations in pitching rate (i.e. second alphabet: medium and slow), the force coefficients exhibit similar behaviour as the Case FF (Fig. 8). From Table 3, it is seen that time averaged force coefficients during Stroke 2 for the three cases are approximately same. Therefore, in subsequent discussion, flow pictures for Case FF is discussed to ascertain the effects of Stroke 1 and flip on Stroke 2.

Case FF is taken as a representative case for discussion on vorticity generated, hence explaining the high force generation. Figs. 12, 13 and 14 show the vorticity plots for the whole cycle where solid

and broken lines represent positive and negative vorticity lines respectively (stroke 1 ending at $\tau = 4.91$, flip ending at $\tau = 6.179$ and stroke 2 ending at $\tau = 11.089$). First Stroke 1 is discussed with the help of vorticity plots at different instants (Fig. 12). It is seen that in the starting phase (see the vorticity plot at the end of the starting phase), a layer of negative vorticity is generated on the upper surface and around the leading edge of the airfoil and a layer of positive vorticity is generated on the lower surface of the airfoil, and the later extends beyond the trailing edge, forming a vortex there (this vortex is called “starting vortex”), i.e. part of this layer has moved away from the airfoil. The negative vorticity

layer forms a vortex at the upper surface close to the leading edge (this vortex is called the “Dynamic Stall Vortex”), which increases in size until $\tau = 1.0$ and afterwards, it remains attached to the surface and does not shed. This explains the absence of stall (C_L and C_D do not vary with time) and managing large value of C_L during constant speed phase. This phenomenon is known as ‘Delayed Stall’.

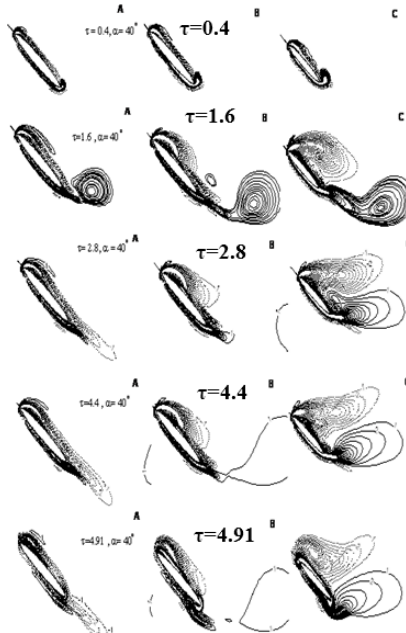


Fig. 12. Vorticity plots for the stroke 1 ($\tau_a = \tau_d = 0.5$ and $\alpha = 40^\circ$) at the three different span locations (A=25%; B=50%; and C=75%) of the wing at different non dimensional time.

As the wing decelerates ($\tau = 4.41$ to $\tau = 4.91$), it is seen that new positive and negative vorticity layers are formed on the upper and lower surfaces of the wing under the previously existing vorticity layers. These new vorticity layers are opposite to that of the acceleration case; this region of newly formed vorticity in a short time explains the negative force coefficients during deceleration.

For the FF case ($\alpha_o^+ = 2.75$), vorticity plots at various angles of attack during flip (pitching motion) are shown in Fig. 13 (after stroke 1 ends at $\tau = 4.91$). As the wing starts to rotate, it can be seen that by $\alpha = 45^\circ$, a new layer of positive vorticity is produced at the upper surface underneath the existing positive vorticity layer produced during the deceleration phase. As the wing pitches up, this vortex layer (positive) curls to form rotation vortex at the leading edge. A positive vorticity at the trailing edge is formed underneath the negative vorticity layer formed during the deceleration phase, which now starts to curl form another positive vortex at the trailing edge. As the fast flip motion continues, these two positive vortices can be seen shedding quickly as the wing approaches $\alpha = 90^\circ$, especially at locations closer to the wing-tip. As the wing rotates beyond $\alpha = 90^\circ$, (pitch down and pitching rate decreases), negative vorticity layers are produced at the upper and lower surfaces. At the

end of rotation, wing surfaces are surrounded by negative vorticity layers while positive vortices are detached / away from the wing.

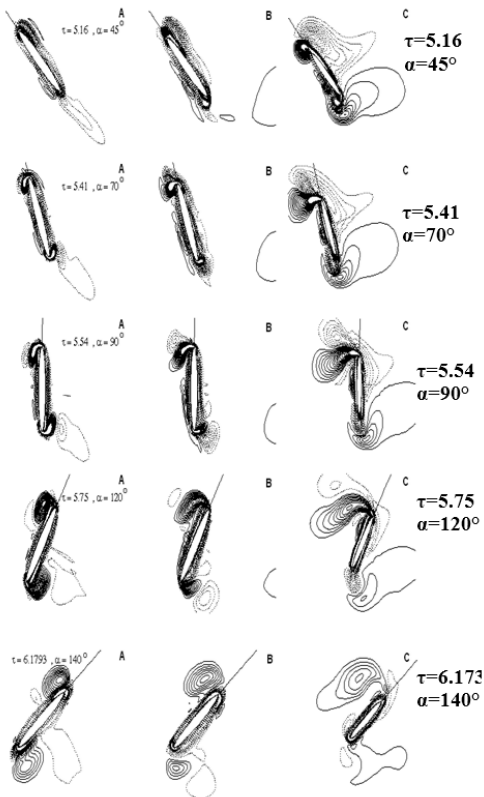


Fig. 13. Vorticity plots for fast flip motion ($\alpha_o^+ = 2.75$ or $\Delta\tau = 1.269$) at the three different span locations (A=25%; B=50%; and C=75%) of the wing at different non dimensional time.

Figure 14 shows the vorticity plot of stroke 2 where it can be seen that the flow around the wing is complex as compared to the stroke 1 (started in still air).

As the wing accelerates, a positive vorticity layer is formed on the upper surface under the negative vorticity layer and a negative vorticity layer is formed on the lower surface. Positive vortices generated during flip are shed at both leading and trailing edge locations, which explains deteriorated performance during acceleration phase of Stroke 2 i.e. the rotational vortices have negative contribution. The negative vorticity on the upper surface, at the end of the flip motion, accumulates at the trailing edge and sheds at the beginning of the Stroke 2. During the constant speed phase, positive vorticity forms the Leading Edge Vortex (LEV) which remains stable. At the trailing edge, negative vorticity generated during the flip combines with the negative vorticity of Stroke 2 forming a negative vortex (starting vortex) which sheds i.e. moves away from the wing. The force generation in stroke 2 is sluggish as compared to stroke 1 due to complex vortex structure especially at the beginning of the stroke (compare vorticity plots of stroke 1 and stroke 2: Figs. 12 and 14). During the

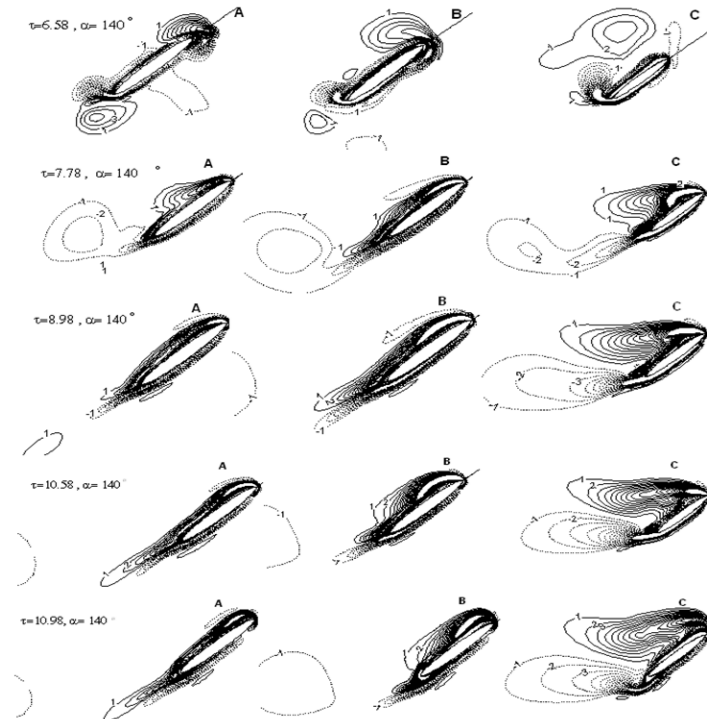


Fig. 14. Vorticity plots for the stroke 2 ($\tau_a = \tau_d = 0.5$) at three span locations (A=25% span location; B=50% span location; C=75% span location) of the wing at different non-dimensional time.

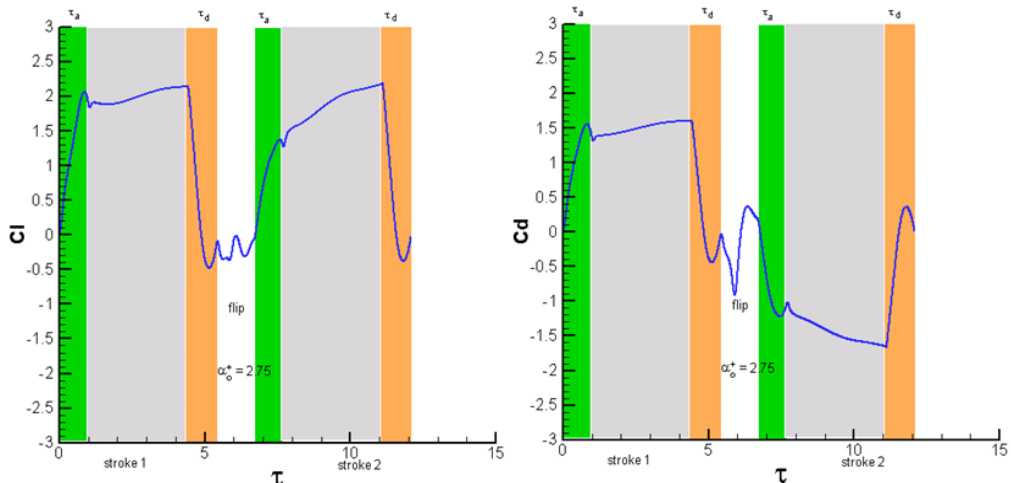


Fig. 15. Case MF: Lift and drag coefficient versus τ during the cycle

$$(\tau_a = \tau_d = 1.0 \text{ and } \alpha_o^+ = 2.75 \text{ or } \Delta\tau_r = 1.269).$$

constant speed phase (lets say at $\tau = 9$ or after 2.5 chord lengths of travel), flow pictures of stroke 1 and stroke 2 are quite similar (Figs. 12 and 14); which explains similar trend of force coefficients for both the strokes after 2.5 chord lengths of travel (Fig. 9).

5.3 Force Production for Cases MF, MM and MS

For repetition, over here first alphabet ‘M’ is for acceleration and deceleration rates during azimuth rotation ($\tau_a = \tau_d = 1.0$) and 2nd alphabet (‘S’, ‘M’, ‘F’) corresponds to flip rates.

Figure 15 shows the instantaneous force production

during the complete cycle for Case MF. It can be seen that during the acceleration phase of Stroke 1, force coefficients closely follow the acceleration rate ($\dot{\psi}^+$) and achieve large force peaks. Peak value of nearly 2.0 for C_L is achieved during acceleration and just after the acceleration ends, C_L drops slightly. From here on, the C_L rises gradually to a new peak and exhibits a large constant value (greater than 2) forming almost a lift plateau during constant speed phase i.e. no sign of stall. Similar variation for C_D is seen from the C_D vs. τ plot in Fig. 8. The behaviour of force coefficients during constant speed phase is quite similar to the previously discussed case (Case FF).

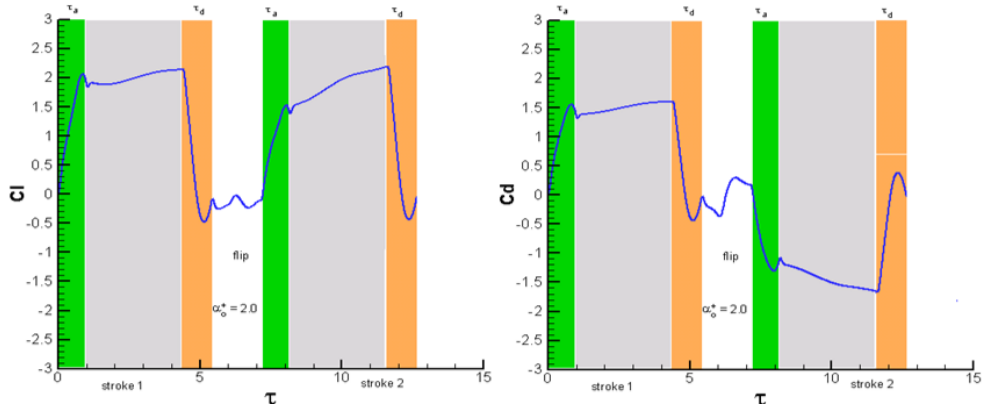


Fig. 16. Case MM: Lift and drag coefficient versus τ during the cycle

($\tau_a = \tau_d = 1.0$ and $\alpha_o^+ = 2.0$ or $\Delta\tau_r = 1.745$).

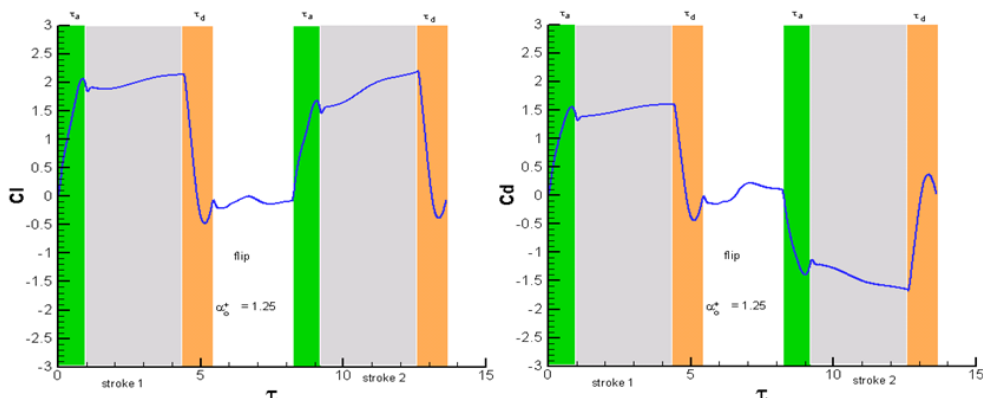


Fig. 17. Case MS: Lift and drag coefficient versus τ during the cycle

($\tau_a = \tau_d = 1.0$ and $\alpha_o^+ = 1.25$ or $\Delta\tau_r = 2.793$).

Table 4 Mean and Maximum force coefficient production during Stroke 1 only, Stroke 1 combined with flip and Stroke 2 only for MF, MM and MS

CASE	MS				MM				MF			
$\tau_a = \tau_d = 1.0$	$\alpha_o^+ = 1.25$				$\alpha_o^+ = 2.0$				$\alpha_o^+ = 2.75$			
	\overline{C}_L	\overline{C}_D	$C_{L\max}$	$C_{D\max}$	\overline{C}_L	\overline{C}_D	$C_{L\max}$	$C_{D\max}$	\overline{C}_L	\overline{C}_D	$C_{L\max}$	$C_{D\max}$
Stroke 1	1.57	1.17	2.07	1.56	1.57	1.17	2.07	1.56	1.57	1.17	2.07	1.56
Stroke 2	1.45	1.12	1.68	1.39	1.43	1.11	1.52	1.30	1.42	1.10	1.37	1.22

The wing then decelerates to zero velocity (end of Stroke 1) where C_L drops immediately and exhibits similar but opposite behaviour to acceleration phase. At the end of Stroke 1, value of C_L is approximately zero. Flipping motion commences during which wing rotates at quarter chord point from $\alpha=40^\circ$ to 140° . During flipping, C_L drops initially to a value of -0.5 and then becomes zero at $\alpha=90^\circ$ and then another peak appears. At the end of flipping motion, C_L is approximately zero.

During acceleration phase of Stroke 2, force coefficients rise rapidly to about 1.25 (which is less than force peak during Stroke 1) and a very slight drop in C_L is observed at the end of acceleration. In the constant speed phase, C_L starts to increase continually till the end of constant speed phase

where it reaches to a value of about 2 while C_D over here is about 1.5.

C_L and C_D versus τ for cases MM and MS are shown in Figs. 16 and 17 respectively. Despite variation in pitching rate (i.e. second alphabet: medium and slow), the force coefficient exhibits similar behaviour as the Case MF (Fig. 15). Table 4 shows the time averaged force coefficients for the 3 cases (MF, MM and MS). The difference between the two strokes is quite visible where Stroke 2 can be seen producing lesser force than Stroke 1 (similar to Case FF, FM, FS).

5.4 Force Production for Cases SF, SM and SS

In the light of preceding discussion, it is seen that

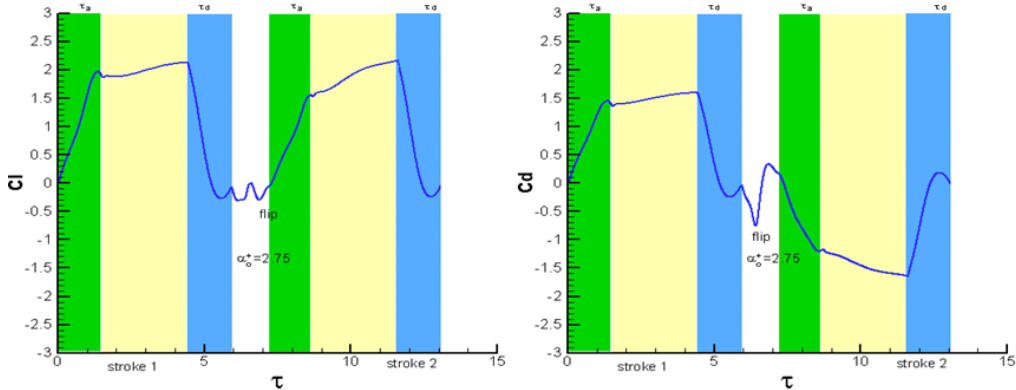


Fig. 18. Case SF: Lift and drag coefficient versus τ during the cycle

($\tau_a = \tau_d = 1.5$ and $\alpha_o^+ = 2.75$ or $\Delta\tau_r = 1.269$).

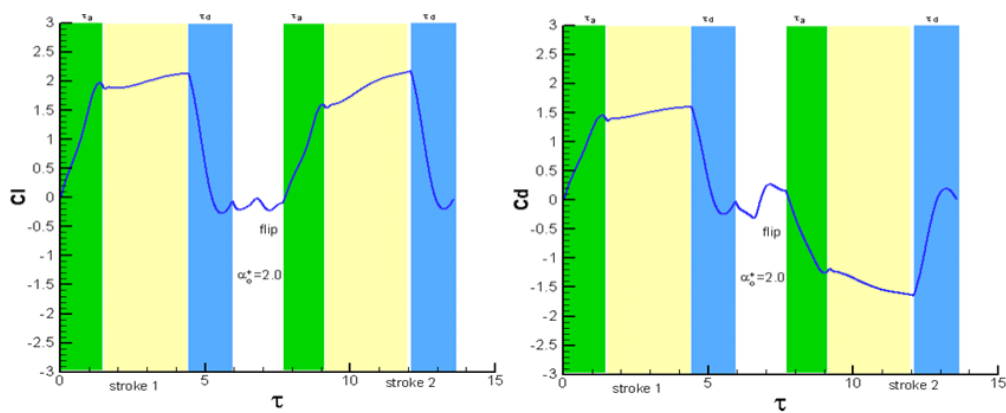


Fig. 19. Case SM: Lift and drag coefficient versus τ during the cycle

($\tau_a = \tau_d = 1.5$ and $\alpha_o^+ = 2.0$ or $\Delta\tau_r = 1.745$).

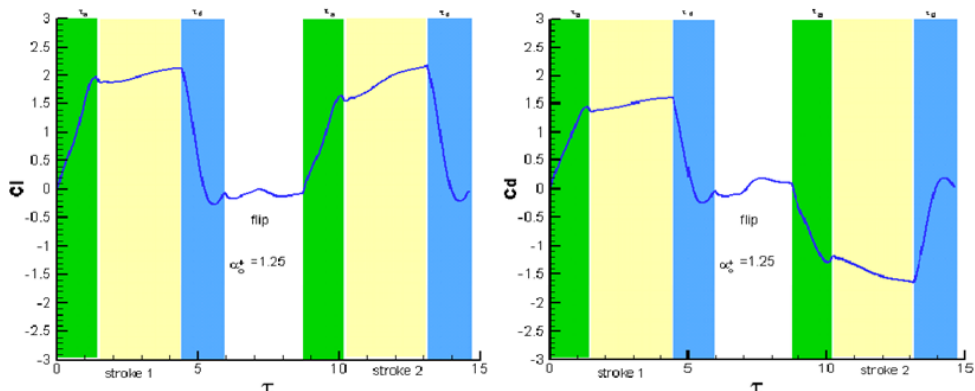


Fig. 20. Case SS: Lift and drag coefficient versus τ during the cycle

($\tau_a = \tau_d = 1.5$ and $\alpha_o^+ = 1.25$ or $\Delta\tau_r = 2.793$).

faster or slower flip rate (2nd alphabet) has similar effect on Stroke 2; therefore all the three cases will be jointly discussed. Figs. 18 to 20 shows the instantaneous force production during the complete cycle for Cases SF, SM and SS respectively. It can be seen that during the acceleration phase of Stroke 1, force coefficients closely follow the acceleration rate ($\dot{\psi}^+$) and achieve large force peaks. C_L peak of nearly 1.97 is achieved during acceleration and just after the acceleration ends, C_L drops very slightly. From here on, the C_L rises slightly and there is forming almost a lift plateau during constant speed

phase i.e. no sign of stall. Similar variation for C_D is seen from the C_D vs. τ plot.

The wing then decelerates to zero velocity (end of Stroke 1), C_L drops immediately and exhibits similar yet opposite behaviour to acceleration phase. At the end of Stroke 1, C_L value is approximately zero. Flipping motion commences during which wing rotates at quarter chord point from $\alpha = 40^\circ$ to 140° . During acceleration phase of Stroke 2, force coefficient rise rapidly to about 1.6 (which is less than force peak during Stroke 1) and only slight drop in C_L is observed by the end of

Table 5 Mean and Maximum force coefficient production during Stroke 1 only, Stroke 1 combined with flip and Stroke 2 only for SF, SM and SS

CASE	SS				SM				SF			
$\tau_a = \tau_d = 1.5$	$\alpha_o^+ = 1.25$				$\alpha_o^+ = 2.0$				$\alpha_o^+ = 2.75$			
	$\overline{C_L}$	$\overline{C_D}$	$C_{L\max}$	$C_{D\max}$	$\overline{C_L}$	$\overline{C_D}$	$C_{L\max}$	$C_{D\max}$	$\overline{C_L}$	$\overline{C_D}$	$C_{L\max}$	$C_{D\max}$
Stroke 1	1.39	1.04	1.97	1.45	1.39	1.04	1.97	1.45	1.39	1.04	1.97	1.45
Stroke 2	1.30	1.00	1.63	1.00	1.29	99	1.60	1.25	1.28	0.98	1.55	1.20

acceleration phase. In the constant speed phase, C_L starts to increase continually till the end of phase reaching to a value of about 2 while C_D reaches to about 1.5.

Table 5 shows the time averaged force coefficients for the 3 cases (SF, SM and SS). The difference between the two strokes is again quite visible where the stroke 2 can be seen producing lesser force than the stroke 1 (similar to previous cases).

6. DISCUSSION

In the light of foregoing, it is seen that during the acceleration phase of Stroke 1 and Stroke 2, force coefficients closely follow the acceleration rate (ψ^+) and achieve large force peaks due to generation and movement of vorticity layers in a short time (acceleration phase); the time rate of change of total first moment of vorticity must be very large which explains the large values of force coefficients in acceleration phase.

During constant speed phase of Stroke 1 (starting in still air), large value of C_L is maintained. A negative vorticity layer forms the dynamic stall vortex at the upper surface close to the leading edge, which increases in size until $\tau = 1.0$ and afterwards, it remains attached to the surface and does not shed. This explains the absence of stall (C_L and C_D do not vary with time) and maintaining a large value of C_L during constant speed phase causing ‘Delayed Stall’. Absence of Stall (or Delayed Stall Mechanism) for a wing performing azimuth rotation has been observed both experimentally and computationally (Sun and Tang (2002a) and Dickinson *et al* (1999)). This mechanism is attributed to the attached leading edge vortex along the span. According to previous studies such as Ellington *et.al* (1996), Van Den Berg *et.al* (1997a) and Van Den Berg *et.al* (1997b), delayed stall mechanism has been attributed to a span wise flow from root to tip. It has been observed in the present study also where there is a strong axial flow from root to tip leading to stability of Dynamic Stall Vortex. The span wise velocity is maintained by the pressure gradient and centrifugal forces due to rotation. It is also seen that the vortex

is more compact at root than near the wing tip because of the wing tip effect.

At the end of Stroke 1, wing decelerates to zero velocity, C_L drops immediately and exhibits similar but opposite behaviour to the acceleration phase. During flipping motion in still air, it is observed that at high rate of angular rotation produces very large force coefficients; however flip preceded by stroke 1 (present case of idealized hovering) does not produce large value of C_L though α_o^+ is quite large. At the end of rotation, wing surface is surrounded by negative vorticity layers while positive vortices are detached / away from the surface.

During Stroke 2, flow around the wing is complex as compared to the stroke 1 (started in still air). The force generation is sluggish as compared to Stroke 1 due to complex vortex structure especially at the beginning of the stroke 2. Comparing Stroke 1 and Stroke 2, the difference between the two strokes is quite visible where Stroke 2 produces lesser force during the acceleration phase and lags in force generation during the constant speed translation phase for nearly 3 chord lengths of travel. In short, Stroke 1 has much more pronounced lift plateau as compared to Stroke 2 which implies that deceleration (at the end of Stroke 1) and flip (stroke reversal) has not contributed positively during the Stroke 2, or in other words, the wake created during the preceding stroke has not influenced positively on Stroke 2.

Variation in acceleration / deceleration rate (first alphabet) from fast to medium to slow shows that the acceleration and deceleration peaks becomes correspondingly smaller and results in smaller value of time averaged force coefficients (Tables 3 and 4). During constant speed phase, wing achieves similar force coefficients irrespective of the acceleration rate and flow pictures are also quite similar to Case FF.

Variation in pitching rate (i.e. from fast to medium to slow), the force coefficients’ behaviour remains unchanged implying that pitch rate has negligible influence on force production during Stroke 2.

Table 6 shows the time averaged force coefficients

and their ratio during Stroke 2 for the 9 cases. It is seen that as flip rate is varied (2nd alphabet), there is only a minor difference in \bar{C}_L and \bar{C}_D . This implies that variation of flip rate from fast, medium to slow (stroke reversal) has similar impact on Stroke 2, or in other words, the negative impact of flipping is independent of the flipping rate. Acceleration / deceleration rate (1st alphabet) has more profound impact as compared to flip rate (2nd alphabet). As the acceleration rate decreases from fast to medium to slow, the time averaged force coefficients show a consistent 10% decrease in \bar{C}_L and \bar{C}_D . This indicates that faster acceleration / deceleration rates (during Stroke 1 and Stroke 2) produce comparatively larger values of \bar{C}_L and \bar{C}_D . More interesting to note from the present study is that \bar{C}_L/\bar{C}_D remains constant at a value of about 1.3 for all the nine cases and thus the aerodynamic efficiency is same for all the 9 cases during idealized hovering motion i.e. independent of acceleration / deceleration or flip rates.

Table 6 Mean force coefficients (\bar{C}_L and \bar{C}_D) and lift to drag ratio for Stroke 2 only

Case	\bar{C}_L	\bar{C}_D	\bar{C}_L/\bar{C}_D
FS	1.62	1.25	1.3
FM	1.60	1.24	1.29
FF	1.59	1.24	1.28
MS	1.45	1.12	1.29
MM	1.43	1.11	1.29
MF	1.42	1.10	1.29
SS	1.30	1.00	1.3
SM	1.29	.99	1.3
SF	1.28	0.98	1.31

7. CONCLUSIONS

At small Reynolds number ($Re=4000$), when wing performs fast acceleration or deceleration motion, large aerodynamic force is generated. During constant speed phase of Stroke 1, there is a lift plateau indicative of delayed stall or attached Dynamic Stall Vortex (DSV). During flip motion between stroke reversals, the force coefficient does not produce large values. In subsequent stroke (Stroke 2), the vortex structure around the wing is complex due to the presence of vortices from Stroke 1 and flipping. During constant speed phase of Stroke 2, in contrast to Stroke 1, force coefficients rise to a constant value is sluggish with the absence of the lift plateau. However, for both the strokes, DSV remains stable and does not shed. The wake formed from stroke 1 and flip influences negatively on the performance during Stroke 2. From all the 9 cases considered in this study, it can be concluded that the aerodynamic efficiency during Stroke 2 remains constant and independent of acceleration / deceleration or the flip rates.

Subsequent research is focused towards analysing

the actual hovering motion with the intent to investigate other high lift generation mechanisms i.e. rotational lift and wake capture.

REFERENCES

- Aono, H., F. Liang and H. Liu (2008). Near- and far-field aerodynamics in insect hovering flight: an integrated computational study. *Journal of Experimental Biology* 211, 239-257.
- Beam, R. M. and R. F. Warming (1978). An Implicit factored scheme for the compressible Navier-Stokes equations. *AIAA Journal* 16, 393-402.
- Birch, J. M., W. B. Dickson, and M. H. Dickinson, (2004). Force production and flow structure of the leading edge vortex on flapping wings at high and low Reynolds numbers. *J. Exp. Biol.* 207, 1063-1072.
- Dickinson, M. H., F. O. Lehmann and S. Sane (1999). Wing rotation and the aerodynamic basis of insect flight. *Science* 284, 1954-1960
- Ellington, C. P. (1984a). The aerodynamics of insect flight. I. The quasi-steady analysis. *Philos. Trans. R. Soc. Lond. B Biol. Sci.* 305, 1-15.
- Ellington, C. P. (1984b). The aerodynamics of insect flight. III. The kinematics. *Philos. Trans. R. Soc. Lond. B Biol. Sci.* 305, 41-78.
- Ellington, C. P. (1984c). The aerodynamics of insect flight. IV. Aerodynamic mechanisms. *Philos. Trans. R. Soc. Lond. B Biol. Sci.* 305, 79-113.
- Ellington, C. P. (1984d). The aerodynamics of insect flight. V. A vortex theory. *Philos. Trans. R. Soc. Lond. B Biol. Sci.* 305, 115-144.
- Ellington, C. P., C. Van Den Berg, A. P. Willmott and A. L. Thomas (1996). Leading-edge vortices in insect flight. *Nature* 384, 626-630.
- Hamdani, H. and M. SUN (2000). Aerodynamic forces and flow structures of an airfoil in some unsteady motions at low Reynolds number. *Acta mechanica* 145(1-4), 1-16.
- Lehmann, F. O. (2004a). The mechanisms of lift enhancement in insect flight. *Nature wissenschaften* 91, 10-122.
- Lehmann, F. O. (2004b). Aerial locomotion in flies and robots: kinematic control and aerodynamics of oscillating wings. *Arthropod Struct. Dev.* 33, 331-345.
- Liu, H. (2002). Computational biological fluid dynamics: digitizing and visualizing animal swimming and flying. *Integr. Comp. Biol.* 42, 1050-1059.
- Liu, H. (2005) Simulation-based biological fluid dynamics in animal locomotion. *ASME Appl. Mech. Rev.* 58, 269-282.
- Liu, H. (2005). Simulation-based biological fluid

- dynamics in animal locomotion. *ASME Appl. Mech. Rev.* 58, 269-282.
- Liu, H. and K. Kawachi (1998). A numerical study of insect flight. *J. Comput. Phys.* 146, 124-156.
- Liu, Y. and M. Sun (2008). Wing kinematics measurement and aerodynamics of hovering drone flies. *Journal of Experimental Biology* 211, 2014-2025
- Liy, H., C. P. Ellington, K. Kawachi, C. VAN DEN BERG and A. P. Willmott (1998). A computational fluid dynamic study of hawk moth hovering. *J. Exp. Biol.* 201, 461-477.
- Naderi, A., M. Mojtabedpoor and A. Beiki (2015). Numerical investigation of non-stationary parameters on effective phenomena of a pitching airfoil at low reynolds number. *Journal of Applied Fluid Mechanics* 9(2), 643-651.
- Sane, S. (2003). The aerodynamics of insect flight. *J. Exp. Biol.* 206, 4191-4208.
- Steger, J. L. (1978). Implicit finite-difference simulation of flow about arbitrary two-dimensional geometries. *AIAA Journal* 16, 679-696.
- Sun, M. and J. Tang (2002a). Lift and power requirements of hovering flight in *Drosophila virilis*. *J. Exp. Biol.* 205, 2413-2427.
- Sun, M. and J. Tang (2002b). Unsteady aerodynamic force generation by a model fruit fly wing in flapping motion. *J. Exp. Biol.* 205, 55-70.
- Sun, M. and X. YU (2006). Aerodynamic force generation in hovering flight in a tiny insect. *AIAA J.* 44, 1532-1540.
- Thomas, P. D. (1982). Composite three-dimensional grids generated by elliptic systems. *AIAA Journal* 20, 1195-1202.
- Van Den Berg, C. and C. P. Ellington (1997a). The three-dimensional leading-edge vortex of a hovering model hawkmoth. *Philos. Trans. R. Soc. Lond. B Biol. Sci.* 352, 329-340.
- Van Den Berg, C. and C. P. Ellington (1997b). The vortex wake of a hovering model hawkmoth. *Philos. Trans. R. Soc. Lond. B Biol. Sci.* 352, 317-328.
- Wang, Z. J. (2005). Dissecting insect flight. *Annu. Rev. Fluid Mech.* 37, 183-210.
- Wang, Z. J., J. M. BIRCH and M. H. Dickinson (2004). Unsteady forces and flows in low Reynolds number hovering flight: two-dimensional computations vs robotic wing experiments. *J. Exp. Biol.* 207, 449-460
- Wu, J. H. and M. SUN (2004). Unsteady aerodynamic forces of a flapping wing. *J. Exp. Biol.* 207, 1137-1150.